The fate of oxygen species resulting from O2 activation at dimetal cofactors in an oXidase enzyme is disclosed by quantum chemistry and 57Fe nuclear resonance X-ray scattering.

Dinesh Kumar Nayak[1], Gobardhan Nayak[2]
[1,2] Gandhi Institute for Education and Technology, Baniatangi, Bhubaneswar

A R T I C L E I N F O

Keywords:
Ferritin
superfamily
Ligand-binding
oXidase Oxygen
activation
Nuclear resonance X-ray
scattering Quantum
chemistry
Isotope labeling

A B S T R A C T

One of the main problems in chemistry is the activation of oxygen (O2), which is catalyzed at prototypical dimetal cofactors in a variety of biological enzymes. Clarifying the chemical pathways of reductive O2 cleavage necessitates the analysis of intermediates. Under varied oxygen and solvent isotopic circumstances, such as 16/18O and H/D exchange, an oXidase protein from the bacterium Geobacillus kaustophilus, R2loX, was employed for aerobic in-vitro reconstitution using only 57Fe(II) or Mn(II) + 57Fe(II) ions to generate [FeFe] or [MnFe] cofactors. Nuclear forward scattering (NFS) and nuclear resonance vibrational spectroscopy (NRVS) data of the R2loX proteins were obtained using 57Fe-specific X-ray scattering methods. Mössbauer quadrupole splitting energies and Fe/Mn(III)Fe(III) cofactor states were revealed by NFS. Molecular structures and vibrational modes were ascribed to the NRVS spectra by quantum chemistry calculations., and protonation patterns of the cofactors, with a metal-bridging hydroXide (μOH−) ligand and a terminal water (H2O) bound at iron or manganese at site 1. A method was created for measuring and comparing the NRVS differential signals from computation and experimentation that result from isotope labeling. This method showed that while 18O from the 18O2 cleavage is incorporated in the hydroXide bridge, the protons of the ligands and the terminal water at the R2loX cofactors interchange with the bulk solvent. In R2loX, a two-step reaction releases the two water molecules from the four-electron O2 reduction into the solvent. In biological and chemical catalysts, these studies establish coupled NRVS and QM/MM for tracking iron-based oxygen activation and elucidate the reductive O2 cleavage mechanism in.

1. Introduction

Enzymes within the ferritin-like superfamily of four-helix-bundle proteins [1–4] incorporate a dimetal-carboXylate cofactor and perform crucial small molecule activation reactions among the top-ten challenges in chemistry [5]. Prominent examples are ribonucleotide reductases essential in DNA synthesis [6–9] and methane monooXygenases catalyzing methane to methanol conversion [10–12] as well as numerous oXidases with widespread functions [13–16].

The classical cofactor comprises two iron ions ([FeFe] type) bound by four glutamate or aspartate and two histidine residues, but in recent years, also di- manganese ([MnMn]) and mixed-metal ([MnFe]) cofactors were dis- covered [13,17–22]. Deeper insight into the reasons for the different metallations [13,23–25] as well as potential variations in reaction pathways at homo- vs. hetero-metallic cofactors [26] is required and may aid the design of improved bimetallic catalysts [27–30].

A common feature of the dimetal cofactors is their high reactivity towards molecular oXygen (O_2) [15,16,31]. Initially divalent metal ions, i.e., Fe(II) or Mn(II), are bound to the apo-proteins and oXidized in the presence of O_2 so that high-valent cofactor species with Mn/Fe(III)/ (IV) ions are formed, which are then employed for amino acid or substrate oXidation reactions to form, e.g., radical species [32–35], on the way to the final products.

The oXygen activation reactions in effect lead to reduction of O_2 by four electrons, resulting in O▌O bond cleavage and in two oXygen species at the formal redoX level of water, with often unknown protonation state (H_2O, OH^-, or O^{2-}) [15,36].

In crystal is employed to probe excitation or annihilation of phonons in the Stokes or anti-Stokes energy regions close to the 57Fe resonance by scanning of a high-re- solution (meV) monochromator for monitoring of vibrational modes.

In addition, nuclear forward scattering (NFS) probes coherent emission interference during decay (lifetime 141 ns) of the I1/2 and I3/2 57Fe excited nuclear spin levels to access Mössbauer parameters (quadrupole splitting energy, ΔEQ, and line width, Γ) in parallel to NRVS spectra [58].

The signals of the $^{18}O_2/D_2O$ protein samples were scaled by a factor of 1.5, to account for only 50% D_2O in these preparations, because the computational data suggested that the H/D exchange contributed about 40–60% to the experimental difference-signals of the samples with simultaneous ^{18}O and D substitutions.

In addition, slight scaling (factors of 1.01–1.04) of the experimental difference signals was applied to compensate for the minor Fe(II) contents in the protein samples. These procedures resulted in consistent NRVS difference- signal data sets for the Fe/Fe and Mn/Fe R2lox preparations (Fig. 8).

For the calculated NRVS spectra of the [FeFe] and [MnFe] cofactors, the QM/MM approach yielded mean difference signal amplitudes, which were overall similar to the experimental data (Fig. S15). The DFT approach yielded about 1.5-fold larger mean signals, but the relative signal amplitudes for the different isotopic patterns were similar to the QM/MM data

Assignment of vibrational bands in NRVS spectra requires normal mode analysis (spectral calculations) based on molecular models as derived from quantum mechanics/molecular mechanics (QM/MM) or density functional theory (DFT) approaches, which was previously established for R2lox and other systems.

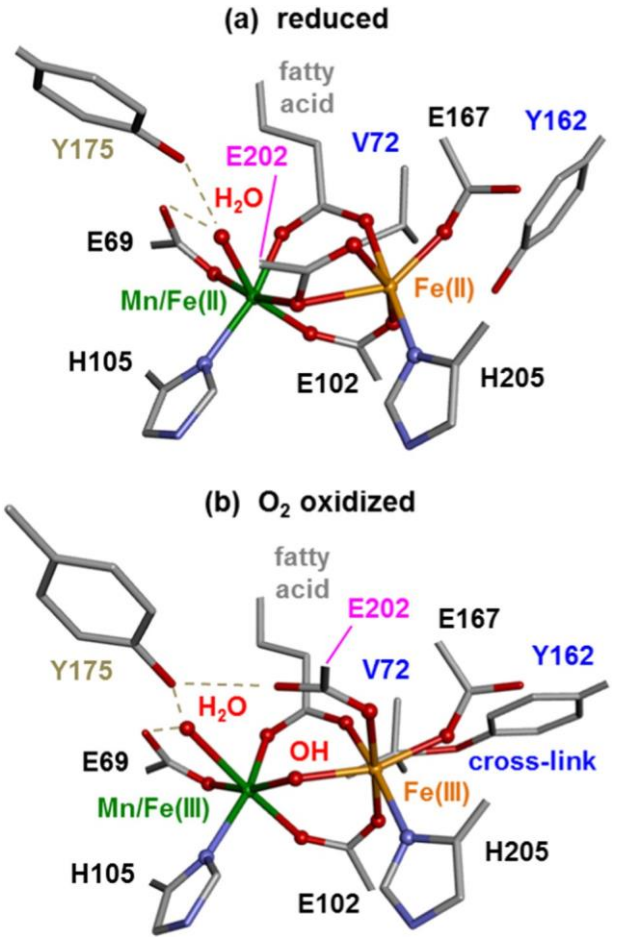

Fig. 1. Crystal structures of [FeFe] and [MnFe] cofactors in R2lox. Geometries are based on PDB entries of (a) anaerobically Mn(II)/Fe(II) reconstituted (reduced) enzymes, 4XBV and 4HR4 ([FeFe], 1.8 Å and [MnFe], 1.9 Å resolution) and (b) aerobically Mn(II)/Fe(II) reconstituted (O_2 oxidized) enzymes, 5OMK and 4HR0 ([FeFe], 1.7 Å and [MnFe], 1.9 Å resolution) [41,43,91]. Color code: green, Fe or Mn in site 1; orange, Fe in site 2; red, O; blue, N; grey, C; protons are not resolved in the protein crystal structures. E202 shows bridging-chelating vs. monodentate metal binding in reduced vs. oxidized structures, the terminal H_2O at Mn/Fe in site 1 is present in all structures, and a bridging oxide as well as a tyrosine-valine ether cross-link is found only in the oxidized structures. A second bridging carboxylate ligand stems from a long-chain fatty acid as modelled in the structures. Dashed lines mark putative hydrogen-bonding interactions at the H_2O and μOH^- ligands.

structures of reduced enzymes, few oxygen species (besides the carboxylate groups) are usually found to be bound to the metal ions whereas in structures of O_2-exposed enzymes, additional oxygen ligands are observed in metal-bridging and/or terminal positions at different dimetal cofactor types [11,37–39] (ref. [15] for review). Whether such species represent the O_2 cleavage products or stem from water molecules (i.e., from the solvent) is a central question of the present study.

Here, we used a structurally characterized ligand-binding oxidase from the bacterium *Geobacillus kaustophilus*, which resembles the R2 subunit of ribonucleotide reductases and is therefore termed R2lox [40–43], as a model system for O_2 activation at [FeFe] and [MnFe] cofactors. Quantitative in-vitro insertion of these cofactor types into apo-protein is feasible [13,43]. Upon supplementation with divalent metal ions and O_2, the enzyme likely forms initial Mn/Fe(IV)Fe(IV) species, followed by oxidation and cross-linking of neighboring tyrosine and valine residues, which results in stable Mn/Fe(III)Fe(III) cofactors (Fig. 1) [41,43–46]. Crystal structures of reduced and oxidized R2lox proteins show varying metal-bridging as well as terminal oxygen species bound at the Fe and Mn ions (Fig. 1) [41,43–45]. Earlier spectroscopic and computational studies have established the ligand protonation state as a terminal water (H_2O) at Mn/Fe in site 1 and a bridging hydroxide (μOH^-) in the Mn/Fe(III)Fe(III) cofactors [40,42,47,48]. Therefore, R2lox is well suited for isotopic labeling experiments for exploration of the origin of the oxygen ligands.

Vibrational spectroscopy is particularly versatile for monitoring ligand binding, exchange, and protonation at metal cofactors [49]. Nuclear resonance (X-ray scattering) vibrational spectroscopy (NRVS) at synchrotron sources is exclusively sensitive to ^{57}Fe sites (^{56}Fe is invisible), so that all vibrational modes of the [MnFe] and [FeFe] cofactors with contributions from the labeled iron centers become accessible, and is unlimited by the selection rules of infrared or Raman spectroscopy [50–54]. The method has rarely been applied to dimetal cofactors [47,55–57]. NRVS relies on the Mössbauer effect, that is, resonant excitation of ^{57}Fe nuclei using ~14.4 keV X-rays to create a 1s level photoelectron due to nuclear excited state decay followed by core hole refill from higher electron levels (e.g., Fe-2p) and X-ray fluorescence photon emission (e.g., Fe Kα at ~6.4 keV). The emission is employed to probe excitation or annihilation of phonons in the Stokes or anti-Stokes energy regions close to the ^{57}Fe resonance by scanning of a high-resolution (meV) monochromator for monitoring of vibrational modes. In addition, nuclear forward scattering (NFS) probes coherent emission interference during decay (lifetime 141 ns) of the $I_{1/2}$ and $I_{3/2}$ ^{57}Fe excited nuclear spin levels to access Mössbauer parameters (quadrupole splitting energy, ΔE_Q, and line width, Γ) in parallel to NRVS spectra [58]. Assignment of vibrational bands in NRVS spectra requires normal mode analysis (spectral calculations) based on molecular models as derived from quantum mechanics/molecular mechanics (QM/MM) or density functional theory (DFT) approaches, which was previously established for R2lox and other systems (see, for example, refs. [40, 42, 47, 53, 54, 59, 60]).

In this study, R2lox apo-protein was in-vitro reconstituted with Mn(II) and ^{57}Fe(II) ions under aerobic and isotopic labeling conditions ($H/D_2{}^{16/18}O$ buffers saturated with $^{16/18}O_2$) and the resulting [^{57}Fe^{57}Fe] and [Mn^{57}Fe] cofactors were investigated by nuclear resonance X-ray scattering. NFS revealed the formation of Mn/Fe(III)Fe(III) cofactors. Different NRVS spectra for the two cofactor types and varying shifts of vibrational bands under the different isotopic conditions were observed. QM/MM calculations facilitated attribution of the NRVS bands to vibrational modes in particular of the terminal water and bridging hydroxide ligands. A quantitative method for correlation of experimental and computational NRVS difference spectra was developed. It assigned the band shifts to individual H/D and/or $^{16/18}$O exchanges, indicating that the terminal water is more rapidly exchangeable than the bridging hydroxide, which stems from O_2. Our findings clarify the O_2 cleavage pathway in R2lox and establish a dedicated method for addressing the reaction coordinate of oxygen activation in iron systems.

2. Materials and methods

2.1. Preparation of R2lox protein and reference samples

$^{57}Fe^{II}Cl_2$ was prepared from metallic ^{57}Fe powder [61]. $^{57}Fe^{II}Cl_2$ (100 or 50 mM, pH 7.0) solution samples (i.e. containing hexaquo ^{57}Fe (II) ions) were prepared in pure H_2O, D_2O, and $^2H\,^{18}O$ or in 50:50 H_2O:D_2O and $H_2{}^{16}O$:$H_2{}^{18}O$ mixtures. Metal-free R2lox apo-protein (pET-46 construct with an N-terminal His_6 tag) was over-expressed in *Escherichia coli* and purified as described previously [43,44,47]. Metal reconstitution, isotopic exchange, and further handling of $^{18}O_2$-exposed R2lox samples was carried out in an anaerobic glove box (MBraun Unilab-Plus-SP, O_2 partial pressure < 10 ppm) and of $^{16}O_2$-exposed R2lox samples was carried out in air (atmospheric O_2 partial pressure). All buffers used in the glovebox for $^{18}O_2$ R2lox sample preparation were deoxygenated by bubbling with N_2 gas for 1 h to remove dissolved O_2

prior to use. For in-vitro metal cofactor assembly, to a solution (500 µL, 811 µM) of R2lox apo-protein 878.5 µL reconstitution buffer (100 mM HEPES-Na, pH 7.0, 50 mM NaCl) were added and for Fe/Fe proteins 121.5 µL of a 10 mM aqueous $^{57}FeCl_2$ solution (concentration ratio protein:Fe 1:3) or for Mn/Fe proteins first 81.0 µL of a 10 mM aqueous $MnCl_2$ solution and then 40.5 µL of a 10 mM aqueous $^{57}FeCl_2$ solution (concentration ratio protein:Mn:Fe 1:2:1) were added (total sample volume 1.5 mL each, protein concentration 270 µM). $^{16}O_2$ samples were incubated in air (atmospheric oxygen) for 1 h at ca. 20 °C whereas $^{18}O_2$ samples were prepared in the glovebox and gently bubbled with a stream of $^{18}O_2$ gas for 4 min prior to the same incubation period. The initially colorless samples showed an immediate color change indicating rapid reaction of the proteins with oxygen and formation of the cofactors with trivalent metal ions. Samples were centrifuged for 4 min (13,000 rpm, 4 °C) and unbound metal ions were removed by passing through a 5 mL HiTrap desalting column (GE Healthcare) equilibrated with 25 mM HEPES-Na buffer (pH 7.0, 50 mM NaCl). The eluate was concentrated by centrifugation (10,000 rpm, Vivaspin-500, 30 kDa cutoff) to a volume of ca. 100 µL. Isotopic labeling of metal-reconstituted R2lox was achieved by buffer exchange using 50% D_2O or 90% $H_2{}^{18}O$ containing buffers (25 mM HEPES-Na, pH 7.0, 50 mM NaCl; diluted from a $H_2{}^{16}O$ buffer stock solution at 10-fold higher concentrations). Protein precipitation at higher D_2O contents limited the maximal D_2O content of R2lox samples to 50% (i.e., each 50% H_2O and D_2O). To 50 µL of the $^{16/18}O_2$ metal-reconstituted R2lox samples, 450 µL of D_2O or $H_2{}^{18}O$ buffer was added, the samples were concentrated as above to ~100 µL, and the buffer addition and concentration procedure was repeated three times (unlabeled O_2/H_2O R2lox was treated in the same way, but with $H_2{}^{16}O$ containing exchange buffer). This procedure yielded the final R2lox samples (Fig. 2; ~50 µL each, protein concentrations given in Tables 1 and S1; 50% D_2O in the $^{16/18}O_2/D_2O$ samples and 90% $H_2{}^{18}O$ in the $^{16/18}O_2/H_2{}^{18}O$ samples). R2lox and $^{57}FeCl_2$ samples were loaded (~50 µL) immediately into Kapton-covered acrylic-glass holders and frozen in liquid nitrogen until use at the synchrotron. Further samples were prepared from additional batches of R2lox protein using comparable preparation procedures with slight variations (e.g., of relative concentrations and incubation periods) in the cofactor reconstitution and isotopic labeling procedures.

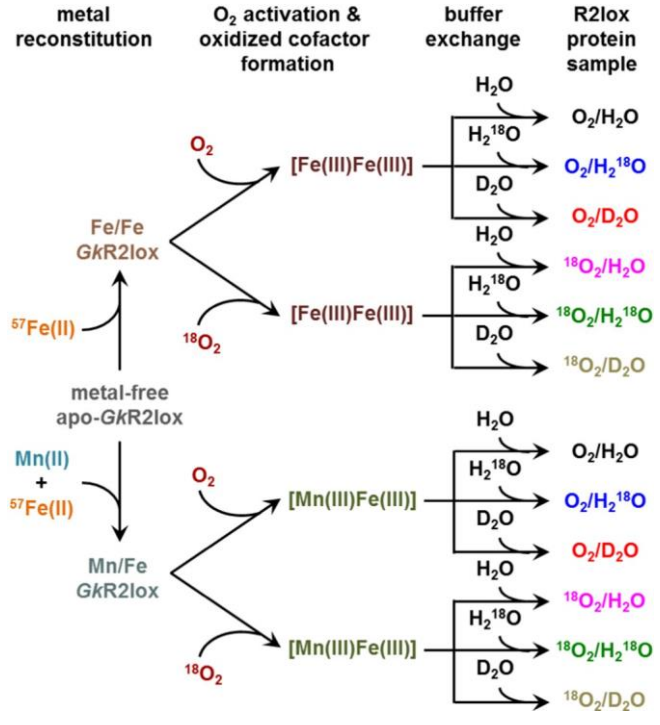

Fig. 2. R2lox protein sample preparation procedure. Metal reconstitution into apo-protein, [FeFe] and [MnFe] cofactor assembly during reductive O_2 activation, and isotopic exchange yielded twelve different R2lox preparations (see Tables 1 and S1 for protein and metal contents and Materials and Methods for details).

2.2. Metal content determination by TXRF

TXRF [62] on a PicoFox spectrometer (Bruker) was employed to determine the metal contents in the actual R2lox protein samples after the nuclear resonance scattering experiments (Fig. S1). A gallium elemental standard (Sigma-Aldrich, 40 mg L^{-1}) was added (1:1 v:v) to the protein samples (7 µL) prior to TXRF analysis, which included the software routines provided with the spectrometer [41,44,47]. Each two measurement repetitions on two independently pipetted samples and averaging of the derived metal contents yielded the values in Tables 1 and S1.

2.3. Nuclear resonance spectroscopy

Nuclear resonance scattering data were collected at undulator beamline ID18 at the European Synchrotron Radiation Facility (ESRF, Grenoble, France) [63] during four beamtime periods (data (a) on a set of 12 R2lox samples prepared by the above main method was collected in one period and further data (b, c, d) on similarly prepared proteins and $FeCl_2$ was collected during the other periods) using the previously described set-up (heat-load monochromator and high-resolution monochromator, FWHM ~0.7 meV; gated APD detectors, ~1 cm^2 active area, for prompt and delayed inelastic and forward scattering detection; cold-finger liquid-helium cryostat) [47,64]. The shown NRVS difference spectra exclusively correspond to spectra that have been collected during one beamtime period (i.e. data (a) in Figs. 4 and 5, see also Figs. S8 and S14) and no averaging of data from different beamtime periods was involved in the analysis. The storage ring was operated in 16-bunch mode (~90 mA). A sample temperature during the measurements of 50 ± 15 K was estimated from the ratio of NRVS counts in ± 3–7 meV windows around the resonance [47]. NFS time traces were collected in a ~160 ns time window within ~30 min with 4 stacked APD detectors at ~2 m behind the sample. NRVS counts were detected with an APD at 90° to the incident X-ray beam and at ~4 mm distance from the sample. The energy axis of the high-resolution monochromator was calibrated using the CN^- vibrational band at 70.0 meV of a $(NH_4)_2Mg^{57}Fe(CN)_6$ powder sample as a reference [65]. NRVS spectra were collected in a −15 meV to 100 meV energy region around the resonance (0.2 meV steps, 3 s per data point, X-ray spot size on sample ~1.5 × 0.5 mm^2). Up to 16 scans were averaged for signal-to-noise ratio improvement (≤4 scans of ~30 min per sample spot). The count background level per second (due to, e.g., electronic noise and imperfectly clean bunch filling of the storage ring) was determined in separate measurements on the samples including data acquisition for 300 s at a ~200 meV off-resonance energy. NRVS data were processed (including background subtraction) and the partial vibrational density of states (PDOS) was calculated with the software package available at ID18. Final NRVS spectra were derived by smoothing of averaged, raw spectra by adjacent averaging over 9 data points (1.8 meV) and interpolation to a 0.4 meV energy step axis, followed by energy to frequency axis conversion (1 meV = 8.06554 cm^{-1}) to give an effective band resolution of ~14 cm^{-1} (full width at half maximum, FWHM). Quadrupole splitting energies (ΔE_Q) were determined from fit analysis of NFS time traces (Eq. (1) with one or two components i, I = NFS amplitude, A_i = amplitude scaling factor, τ_i = effective decay lifetime, υ_i = modulation frequency, ϕ = phase shift, B = detector count offset; $\Delta E_Q = h\upsilon$ with $h = 4.135 \times 10^{-6}$ neV s) [66–68]:

$$I_{NFS}(t) = \sum A_i \exp(-t_i/\tau_i)\cos^2(\pi\nu_i t + \phi) + B. \quad (1)$$

The apparent Mössbauer linewidth (Γ) was calculated from the τ

Table 1
Mean metal contents and Mössbauer parameters of R2lox protein samples.[a]

R2lox protein	Mn per protein	Fe per protein	Mn per Fe	M per protein	[FeFe] [%]	[MnFe] [%]	[MM] per protein	Fe(II) [%]	ΔE_Q Fe(III) [mm s^{-1}]	Γ Fe(III) [mm s^{-1}]
Fe/Fe	< 0.01(1)	1.92(7)	< 0.01(1)	1.92(7)	> 99(1)	< 1(1)	0.96(4)	2.8(1.3)	0.79(1)	0.38(2)
Mn/Fe	0.61(3)	0.79(4)	0.77(6)	1.40(11)	13(4)	87(4)	0.70(6)	2.8(1.7)	0.83(2)	0.52(9)

[a] Metal contents were determined by TXRF (Fig. S1). Mössbauer parameters (quadrupole splitting energy, ΔE_Q; line width, Γ) of Fe(III) species and Fe(II) contents were determined from NFS data (Figs. 3, S2). The mean protein concentration was 4.2 mM, full parameter variation ranges over all protein samples are given in parentheses, for parameters of the individual samples see Tables S1 and S2. [FeFe] and [MnFe] cofactor contents were calculated under the assumption that all manganese ions are bound in [MnFe] cofactors (M and [MM] denote the sums of metal ions and dimetal cofactors per protein). Other first-row transition metals were negligible in all protein samples (Table S1).

values (Eq. (2); excited state lifetime, $\tau_0 = 141$ ns; 1 mm $s^{-1} = 4.8 \times 10^{-5}$ meV):

$$\Gamma = h/2\pi(1/\tau_0 + 1/\tau) \quad (2)$$

We note that the small sample thickness in the NFS experiment on dilute protein solutions containing ^{57}Fe in the cofactors most likely does not lead to dynamical beats due to multiple scattering contributions to the time traces, but the pattern is practically exclusively due to the double-resonance quadrupole splitting. This follows from the observation that the given sample conditions (~5 mm X-ray path through the sample, ~5 mM average ^{57}Fe concentration) would correspond to a ^{57}Fe metal foil of < 0.2 μm thickness, for which no dynamical beats are observed according to data in literature [58,69–72]. This assumption is further evidenced by the similar Mössbauer parameters that were determined from protein samples with ^{57}Fe concentrations that varied up to a factor of 2 (Tables S2, S3, S4). We therefore conclude that multiple-scattering effects in the NFS traces are negligible and the relative Fe(III) and Fe(II) amounts are reliably determined (estimated error ± 5%, Table S4).

2.4. QM/MM calculations

Calculations were carried out on the computer clusters of Freie Universität Berlin and based on whole-protein/cofactor model structures as constructed using R2lox crystal structures and our earlier experimental and computational results (Fig. 1). A QM/MM approach including ONIOM [73,74] and the universal force field as implemented in the Gaussian09 program [75] were used for the MM treatment of the protein environment (low-layer) and the B3LYP functional [76,77] with the TZVP basis-set [78] was used for the QM core (high-layer including the dimetal cofactor and adjacent amino acids) for unconstrained geometry-optimization and spectral calculations. In addition, DFT calculations with the same functional/basis-set combination were carried out on models including only the cofactors (metal ions plus truncated amino acid ligands and water species). A broken-symmetry approach and proper assignment of molecular fragments were used for calculation of anti-ferromagnetic spin couplings [47,64,79,80]. The total spin multiplicity (M = 2S + 1) was 1 (S = 0) for the diamagnetic Fe(III)Fe(III) cofactor and 2 (S = ½) for the paramagnetic Mn(III)Fe(III) cofactor [42,43,47]. NRVS vibrational frequencies were derived from normal mode analysis of relaxed structures using Gaussian09. NRVS and normalized (spectral area = 1) PDOS spectra were calculated using NISspec [81]. Calculated (stick) NRVS spectra were broadened by Lorentzians (FWHM 14 cm^{-1}) for comparison with experimental spectra. In-house software and functionalized EXCEL-sheets were used to process Gaussian09 and NISspec output files. NRVS vibrational modes were visualized with ChemCraft.

2.5. Correlation of experimental and computational NRVS difference spectra

NRVS difference spectra were calculated from the experimental and computational data (spectra of isotope-exchanged cofactor species minus spectra of unlabeled, i.e., H_2O/μOH cofactor species). Experimental NRVS difference spectra were smoothed over 5 data points for display. Quantification of experimental, normalized NRVS difference spectra (PDOS) was carried out using Eq. (3). First, their modulus was calculated and the resulting spectra were integrated (if not stated otherwise) in a 100–550 cm^{-1} spectral range, ΔF_{SB}, to yield the area corresponding to the signal-plus-background level (SB, in %) and in a 600–750 cm^{-1} spectral range, ΔF_B, without significant band features to yield the area corresponding to the background (noise) level (B, in %). Subtraction of the background level after scaling by a factor, $X = \Delta F_{SB} / \Delta F_B$, of 3 (to compensate for its 3-fold shorter frequency range) from the signal-plus-background level resulted in the NRVS difference signal (S, in %), which included most of the significant vibrational band features:

$$S = \int \mathrm{mod}(SB)_{\Delta FSB} - \int \mathrm{mod}(B)_{\Delta FB} \cdot X \,. \quad (3)$$

A similar procedure was applied to the computational (i.e., noise free) NRVS difference spectra, but omitting the background subtraction, to yield the calculated NRVS difference signal. The following scaling factors were applied to the resulting experimental NRVS difference signals (for Fe/Fe and Mn/Fe proteins) for comparison with the computational data (see Fig. S10 for further justification of the scaling factors): x2 for the $^{16}O_2/D_2O$ proteins to compensate for the presence of only 50% D_2O, x1.5 for the $^{18}O_2/D_2O$ proteins to compensate for the presence of only 50% D_2O and assuming a 50% contribution of the H/D exchange to the total NRVS difference signal according to the calculation results, and x1.1 for the $^{16/18}O_2/H_2{}^{18}O$ proteins to compensate for the presence of only 90% $H_2{}^{18}O$ (x1 for the other difference signals). The root-mean-square deviation (rmsd) between experimental and calculated NRVS difference signals (S) was calculated using Eq. (4):

$$rmsd = \sqrt{(S_{cal} - S_{exp})^2} \,. \quad (4)$$

3. Results

3.1. Isotopic labeling and metal content of R2lox

Purification of metal-free R2lox apo-protein, followed by addition of Mn(II) and ^{57}Fe(II) ions or only of ^{57}Fe(II) ions, reconstitution of the oxidized [MnFe] and [FeFe] cofactors during exposure to $^{16}O_2$ or $^{18}O_2$ and exchange of buffers containing water isotopes (see Materials and Methods), resulted in twelve concentrated (ca. 3.0–5.5 mM), completely ^{57}Fe labeled holo-protein samples for nuclear resonance scattering experiments denoted further on: O_2/H_2O, O_2/D_2O, $O_2/H_2{}^{18}O$, $^{18}O_2/H_2O$, $^{18}O_2/H_2{}^{18}O$, and $^{18}O_2/D_2O$ (Fig. 2). Metal contents of the R2lox samples were determined by TXRF (Fig. S1; Tables 1, S1). In the Fe/Fe-reconstituted R2lox samples, negligible manganese and near-stoichiometric iron binding was found (mean of 1.9 ± 0.1 Fe ions or 0.95 ± 0.05 [FeFe] cofactors per protein). The Mn/Fe-reconstituted proteins contained slightly sub-stoichiometric metal (mean of 1.4 ± 0.2 metal ions or 0.70 ± 0.10 dimetal cofactors per protein) and 0.75 ± 0.10 Mn ions per Fe ion on average, from which mean

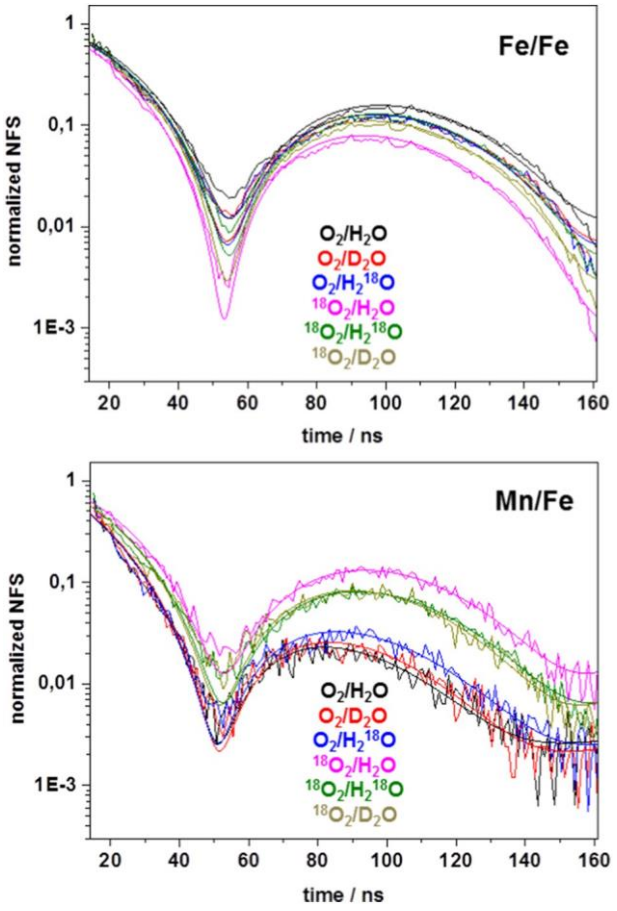

Fig. 3. NFS time traces of R2lox protein samples. Experimental data (top panel, Fe/Fe samples; bottom panel, Mn/Fe samples) are shown together with fit curves (smooth lines, parameters in Tables 1 and S2). Traces were normalized to an initial amplitude of unity at zero time according to the fit results, note the logarithmic scaling of the y-axes.

[MnFe] and [FeFe] cofactor contents of 87 ± 4% and 13 ± 4% were calculated (Table 1). Only small and unsystematic metal loading (± 10%) and cofactor content (± 5%) variations were observed for the Fe/Fe and Mn/Fe samples exposed to the different isotopic conditions. Earlier Mössbauer and EPR data on similar R2lox samples have shown that unspecific Fe(III) contaminations are negligible [40,42,47]. These results reveal the efficient and selective formation of [FeFe] and [MnFe] cofactors in R2lox, which is practically independent of reconstitution in the presence of $^{16}O_2$ or $^{18}O_2$, as well as unaffected by subsequent H/D_2 $^{16/18}O$ buffer exchange.

3.2. Cofactor redox state and Mössbauer parameters

Nuclear forward scattering (NFS) nanosecond transients were collected for the twelve different R2lox samples (Fig. 3). For selected isotopic conditions, further NFS transients of independently prepared R2lox samples were obtained (Fig. S2). Overall similar kinetic behavior of the Fe/Fe and Mn/Fe samples was observed, featuring rapid NFS amplitude decay and oscillation with a low frequency [47]. These properties were only marginally affected by the different sample preparation procedures including O_2 and water isotopes. For comparison with the R2lox data reflecting mostly Fe(III) species (see below), NFS transients were recorded for $^{57}FeCl_2$ solutions containing hexaquo-Fe (II) ions as prepared with H_2O, D_2O, or $H_2{}^{18}O$ (Fig. S3). These transients revealed a much larger amplitude oscillation frequency of the solution Fe(II) ions compared to the Fe(III) species in R2lox, which was not affected by the isotopic conditions. In addition, NFS transients were recorded for Fe/Fe and Mn/Fe R2lox samples (O_2/H_2O) directly after prolonged X-ray exposure (~2 h) at ~50 K or after annealing the same samples at ~220 K for 1 h (Fig. S4). The annealing was expected to cause reduction of protein-bound metal(III) to metal(II) species due to reaction of X-ray induced protein and solvent radical species, which are trapped at 50 K, with the cofactors at 220 K [47,82]. Accordingly, the NFS transients of the annealed R2lox samples showed an overlay of amplitude oscillations with lower and higher frequencies.

Fit analysis of the NFS transients using Eqs. (1) and (2) (with one or two kinetic phases) provided the relative amounts of divalent and trivalent iron species in the R2lox samples as well as Mössbauer parameters, that is, the quadrupole splitting energy, ΔE_Q, and the apparent line width, Γ (Figs. 3, S2; Tables 1, S2). The Mössbauer parameters of hexaquo-Fe(II) in the $^{57}FeCl_2$ solutions were typical for ferrous iron [83] and barely affected by the presence of only H_2O or 50/100% D_2O or 50/100% $H_2{}^{18}O$, as well as by concentration variation (50 mM vs. 100 mM Fe) (Table S3, mean values of $\Delta E_Q = 3.24 \pm 0.01\ mm\ s^{-1}$ and $\Gamma = 0.71 \pm 0.05\ mm\ s^{-1}$). The transients of annealed Fe/Fe and Mn/Fe R2lox both revealed a ~33% NFS contribution with Mössbauer parameters due to Fe(II) (Table S4, mean values of $\Delta E_Q = 2.60 \pm 0.05\ mm\ s^{-1}$ and $\Gamma = 0.50 \pm 0.02\ mm\ s^{-1}$) that differ from the $^{57}FeCl_2$ values, which implies that the formed Fe(II) was still bound to the cofactor sites in R2lox. Simulations of the NFS transients of the corresponding non-annealed R2lox samples showed that a respective Fe(II) contribution was very small (≤5%), indicating the mere absence of X-ray induced reduction of the dimetal cofactors during nuclear resonance scattering data collection as well as no significant residual divalent iron in the samples from the metal reconstitution.

Simulations of the NFS transients of R2lox for the various isotopic conditions (Figs. 3, S2) revealed slightly different Mössbauer parameters for Fe(III) in the Fe/Fe or Mn/Fe proteins (Tables 1, S2), namely mean values of (Fe/Fe) $\Delta E_Q = 0.79 \pm 0.01\ mm\ s^{-1}$ and $\Gamma = 0.38 \pm 0.02\ mm\ s^{-1}$ and (Mn/Fe) $\Delta E_Q = 0.83 \pm 0.02\ mm\ s^{-1}$ and $\Gamma = 0.52 \pm 0.09\ mm\ s^{-1}$. These values were practically independent of the isotopic conditions and well reproducible in independently prepared protein samples (Fig. S5). The larger Γ for Mn/Fe R2lox is mostly attributed to contributions from the minor amounts of [FeFe] sites, as judged from a weak correlation of Γ with the [FeFe] cofactor percentage in the Mn/Fe samples (Fig. S6). Although the Fe(II) contributions were very small (≤5%) in all samples (Fig. S7), the Fe/Fe protein showed larger Fe(II) amounts in the non-$^{18}O_2$ samples, while the Mn/Fe protein showed larger Fe(II) amounts in the $^{18}O_2$ samples, which mostly explained the visual deviations between the respective NFS transients of Mn/Fe and Fe/Fe R2lox (Fig. 3). In summary, the NFS data indicated the presence of almost exclusively Fe(III)Fe(III) cofactors in the Fe/Fe proteins and, taking into account also our earlier quantifications of Mn(III) [40,44,47], of Mn(III)Fe(III) cofactors in the Mn/Fe proteins.

3.3. NRVS analysis of isotope effects in R2lox

NRVS spectra of the Fe/Fe and Mn/Fe R2lox samples were collected (Figs. 4, S8). Significant differences of relative amplitudes and frequencies of vibrational bands were observed for the Fe/Fe vs. Mn/Fe samples, which reflect the presence of two different Fe(III) sites in the [FeFe] cofactors compared to Fe(III) only in site 2 in the [MnFe] cofactors (besides the minor [FeFe] amounts in Mn/Fe R2lox, Fig. S9). For the various isotopic conditions, overall similar NRVS spectra were observed, which revealed relatively small band shifts mostly to lower frequencies (on the order of ~5 cm^{-1} or less, e.g., for the main band at ~250 cm^{-1}) compared to the O_2/H_2O samples, as visible in the respective difference spectra (Figs. 4, S8). The main band shift directions suggested isotopic exchange at the cofactors because lower vibrational frequencies were expected for the H_2O and μOH ligands including the heavier ^{18}O and/or D atoms. However, the difference spectra also showed sizeable background (noise) contributions, as discernable, e.g.,

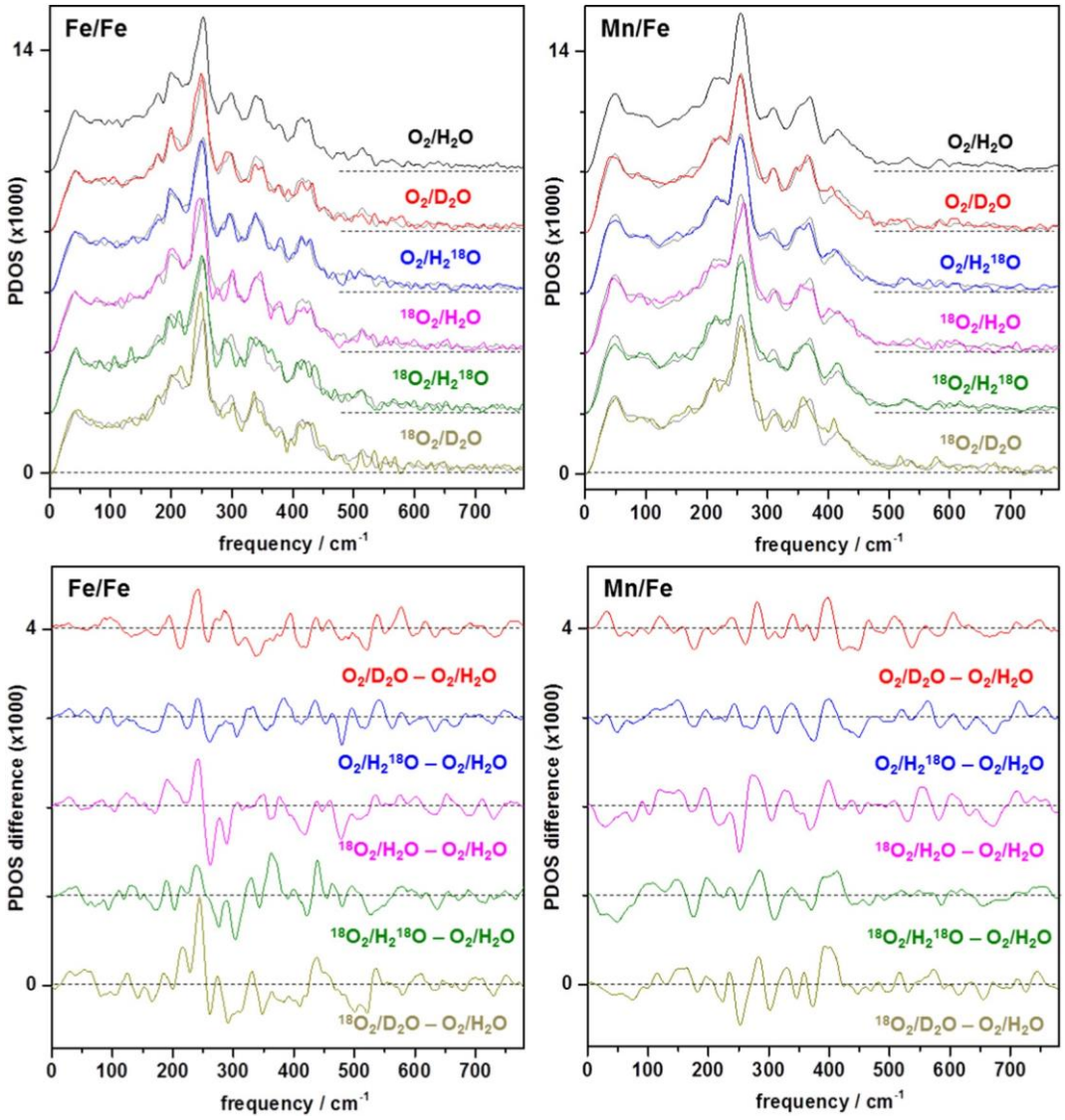

Fig. 4. NRVS spectra of R2lox protein samples. Top panels, NRVS spectra (PDOS) and bottom panels, NRVS difference spectra of Fe/Fe samples (left) and Mn/Fe samples (right). Spectra are vertically displaced for comparison (grey lines show shifted spectra of O_2/H_2O protein samples, dotted lines mark respective baseline levels). The maximal noise level in the NRVS spectra or difference-spectra is estimated from the spectral levels above ca. 600 cm^{-1} where no real bands occur as ~5% or 20% of the maximal amplitudes at lower frequencies (smaller relative noise levels are expected at lower frequencies due to the exponentially increasing weighting of data at increasing frequencies in the NRVS evaluation).

in the $> 550\ cm^{-1}$ frequency region where no significant vibrational bands were observed (Figs. 4 and 5), even after averaging of all Fe/Fe or Mn/Fe spectra to further decrease the noise level (Fig. S9). Accordingly, for discrimination of the actual site of isotope exchange at the cofactors, a method for quantification of the small band shift features was needed. For this purpose, NRVS spectra of the $^{57}FeCl_2$ samples were re- corded, which showed significant ($\leq 15\ cm^{-1}$) band downshifts for hexaquo-Fe(II) in D_2O or H ^{18}O vs. H O (Fig. S10). Visual inspection reproduced the expected difference-spectra amplitude changes by a factor of two with about ± 5% accuracy even for largely (3-fold) di- verging background contributions to the NRVS spectra (Fig. S10, mean relative error of the D_2O - H_2O and H ^{18}O – H_2O difference signals of ca. 10%). In the following, this method for difference-spectra quantification was applied to compare experimental and theoretical NRVS data of R2lox.

revealed overall twice as large amplitudes of the difference spectra for 100% instead of 50% D_2O or $H_2{}^{18}O$ in the samples, as expected due to H/D or $^{16}O/^{18}O$ exchange in the complete or (on average) half of the water ligand sphere at the $^{57}Fe(II)$ ions. The integral of the modulus of the difference spectra was calculated (Eq. (3)) in two spectral regions where only background (noise) contributions or also vibrational bands were present, and the weighted background amplitudes were subtracted from the total background plus signal amplitudes, which yielded the true differential-signal amplitudes. This procedure resulted in signal amplitudes due to vibrational band shifts in the $^{57}FeCl_2$ samples, which

Two quantum chemical approaches (QM/MM and DFT) [47] based on crystal structures of the whole R2lox protein/cofactor system or only of the cofactor/amino-acid ligands (Fig. S11) were used to calculate NRVS spectra for eight different isotopic labeling patterns of the bridging hydroxide and terminal water ligands (OH/H_2O, OD/D_2O, OH/H ^{18}O, $^{18}OH/H$ O, $^{18}OH/H$ ^{18}O, OD/D ^{18}O, $^{18}OD/D$ O, $^{18}OD/D$ ^{18}O) at the [FeFe] and [MnFe] cofactors (Figs. 6, S12). The QM/MM spectra reproduced the broad background due to coupled protein/cofactor modes, the relative intensities of the main NRVS band features, as well as the differences between the spectra of Fe/Fe and Mn/Fe proteins (Fig. S13) in the experimental data reasonably well (and better than the DFT spectra). The absence of prominent band features above about

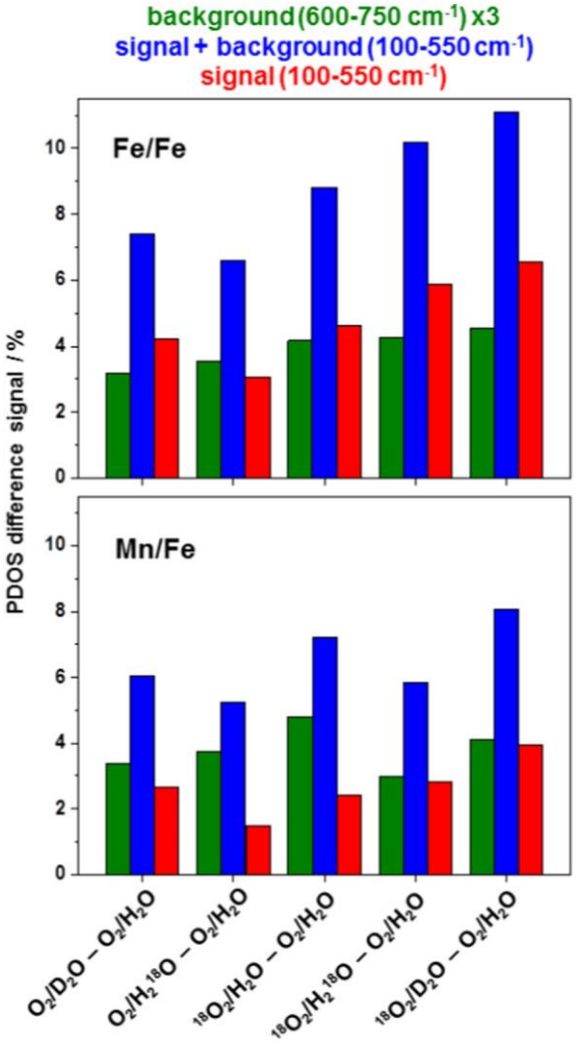

Fig. 5. Quantification of NRVS difference signals of R2lox samples. (A) Indicated NRVS difference signals for Fe/Fe (top panel) and Mn/Fe (bottom panel) R2lox samples with isotopic exchanges derived from NRVS (PDOS) spectra in Fig. 4 using Eq. (3) (frequency ranges of ΔF_{SB}, 100–550 cm^{-1} and ΔF_B, 600–750 cm^{-1} and a scaling factor X of 3). For further NRVS difference signals see Fig. S14 (data shown here correspond to data (a) in Fig. S14; the mean relative error of the difference signals was estimated from up to three measurements of independent samples with the same isotopic composition to be ca. 12%).

550 cm^{-1} in the calculated and experimental spectra (Figs. 4 and 5) confirmed the earlier determined protonation state of the [FeFe] and [MnFe] cofactors with a terminal water (H_2O) at the metal in site 1 and a bridging hydroxide (μOH^-) [42,47]. It further showed that above 550 cm^{-1}, background contributions dominate the experimental spectra. For the different isotopic labeling patterns overall similar NRVS band shifts were observed in the QM/MM and DFT difference spectra, despite the deviations in relative NRVS band intensities (Figs. 6, S12). In particular, the difference spectra for the [FeFe] cofactor showed prominent (ca. 3–22 cm^{-1}) band down-shifts in mainly three spectral regions (around 260 cm^{-1}, 380 cm^{-1}, and 470 cm^{-1}), whereas the difference spectra for the [MnFe] cofactor showed overall smaller ($\leq$5 cm^{-1}) band down-shifts in mainly two regions (around 300 cm^{-1} and 400 cm^{-1}).

NRVS vibrational modes with prominent contributions of the H_2O and μOH ligands at the cofactors were identified by inspection of the computational output files (stick spectra), each including more than 5000 normal modes (Fig. 7). For the [FeFe] and [MnFe] cofactors, distinct variations in the frequencies of such vibrations were observed, but for both cofactors, coupled vibrations with contributions from both ligands were found around 275 cm^{-1}, vibrations with mainly H_2O contributions occurred in the 300–360 cm^{-1} region, and prominent vibrations with mainly μOH^- contributions were scattered over the 360–400 cm^{-1} and 480–530 cm^{-1} regions (Fig. 7). We note, however, that coupled vibrations with weak contributions from both ligands were spread over the entire spectral regions showing significant NRVS band features. These findings implied that analysis of only a few (prominent) band shift features in the experimental NRVS spectra of the isotope-exchanged R2lox samples is not sufficient, but that the whole (difference-) spectra need to be taken into account for reliable discrimination of different H/D and $^{16}O/^{18}O$ labeling patterns.

3.4. Quantification of experimental and computational NRVS difference signals

We applied the quantification method described above to the experimental and calculated isotopic NRVS difference spectra of R2lox (Figs. 4, 5 and S8, S12). The resulting NRVS difference signal amplitudes are shown in Figs. 6, 8 and S14, S15. For the experimental data of the Fe/Fe and Mn/Fe samples (Fig. 4), similar relative signal amplitudes of the difference spectra were observed, with an about 2-fold smaller $O_2/H_2{}^{18}O - O_2/H_2O$ signal compared to the similar $O_2/D_2O - O_2/H_2O$ and $^{18}O_2/H_2O - O_2/H_2O$ signals and (up to 1.5-fold) larger signals of the $^{18}O_2/H_2{}^{18}O - O_2/H_2O$, and, in particular, $^{18}O_2/D_2O - O_2/H_2O$ differences (Figs. 6 and S14). For the further R2lox protein preparations (Fig. S8), even for pronounced (≤10-fold) noise level variations in the NRVS spectra, the relative as well as the absolute signal amplitudes were well reproducible (within less than ± 10% margins, Fig. S14). On average, the difference signals of the Fe/Fe samples were about twice as large as the signals of the Mn/Fe samples, with only minor variations (Mn/Fe:Fe/Fe, 0.5 ± 0.1:1). These results indicate significant alterations in the difference signal amplitudes due to the varying isotopic substitutions. For comparison with the computational data, the experimental difference signals of the O_2/D_2O and $O_2/H_2{}^{18}O$ R2lox samples were scaled by factors of 2.0 and 1.1 to compensate for the sub-stoichiometric (50% or 90%) D_2O or $H_2{}^{18}O$ contents in the preparations, which, according to the $^{57}FeCl_2$ results (above), was expected to cause isotopic labeling of only 50% or 90% of the cofactors on average. The signals of the $^{18}O_2/D_2O$ protein samples were scaled by a factor of 1.5, to account for only 50% D_2O in these preparations, because the computational data suggested that the H/D exchange contributed about 40–60% to the experimental difference-signals of the samples with simultaneous ^{18}O and D substitutions. In addition, slight scaling (factors of 1.01–1.04) of the experimental difference signals was applied to compensate for the minor Fe(II) contents in the protein samples. These procedures resulted in consistent NRVS difference-signal data sets for the Fe/Fe and Mn/Fe R2lox preparations (Fig. 8).

For the calculated NRVS spectra of the [FeFe] and [MnFe] cofactors, the QM/MM approach yielded mean difference signal amplitudes, which were overall similar to the experimental data (Fig. S15). The DFT approach yielded about 1.5-fold larger mean signals, but the relative signal amplitudes for the different isotopic patterns were similar to the QM/MM data (Fig. S15). Both approaches revealed similar relative signal amplitudes for the corresponding isotopic patterns in the [FeFe] and [MnFe] cofactors, with the smallest signal seen for the $OH/H_2{}^{18}O - OH/H_2O$ difference, about 2-fold larger and similar signals for the $OD/D_2O - OH/H_2O$, $^{18}OH/H_2O - OH/H_2O$, $^{18}OH/H_2{}^{18}O - OH/H_2O$, and $OD/D_2{}^{18}O - OH/H_2O$ differences, and increasingly larger signals for the $^{18}OD/D_2O - OH/H_2O$ and $^{18}OD/D_2{}^{18}O - OH/H_2O$ differences. Similar to the experimental data, on average 2-fold larger [FeFe] vs. [MnFe] signals were found. Merging the QM/MM and (scaled) DFT data provided computational NRVS difference-signal data sets of the [FeFe] and [MnFe] cofactors (Fig. 8). Visual comparison of the experimental and computational NRVS difference signals already showed that the overall

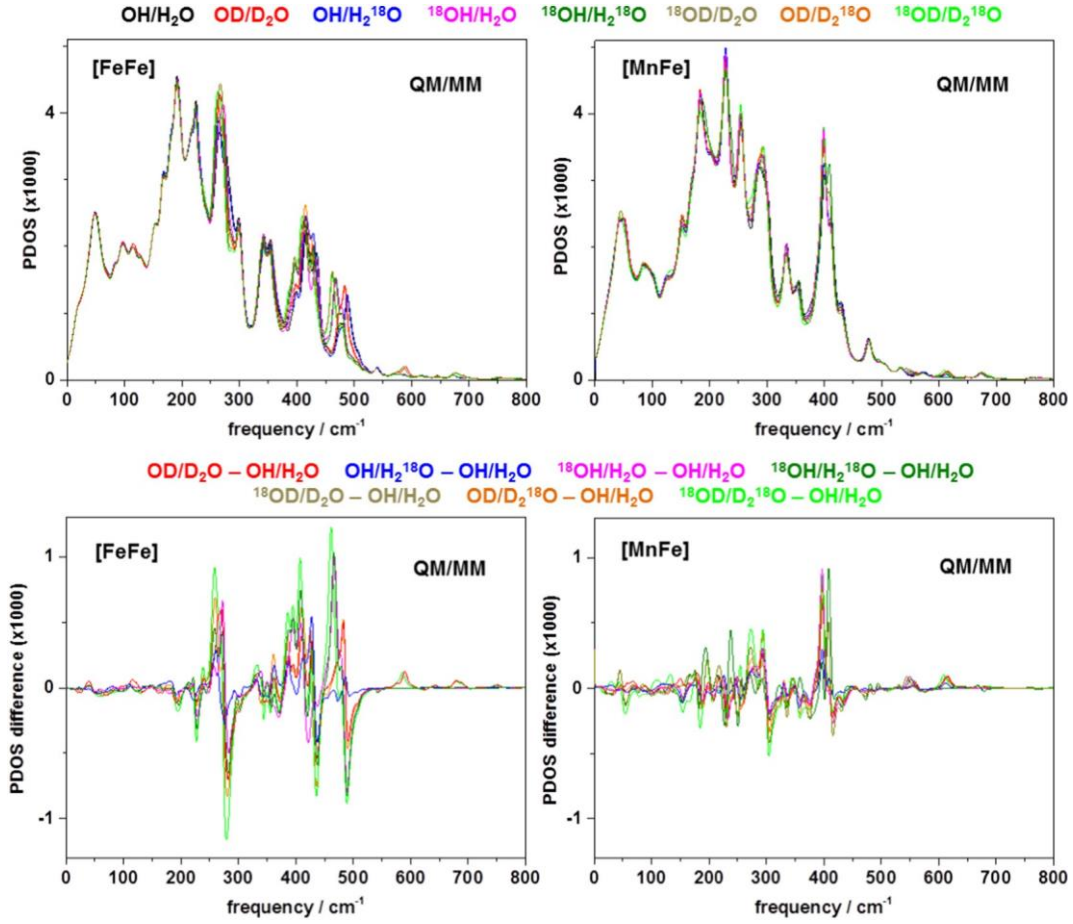

Fig. 6. Computational NRVS spectra from QM/MM. Top panels, NRVS spectra (PDOS) and bottom panels, NRVS difference spectra of R2lox protein structures with [FeFe] cofactors (left) or [MnFe] cofactors (right). The respective isotopic labeling patterns are indicated, for example OH/H_2O refers to cofactor structures with a metal-bridging $\mu^{16}OH^-$ and a terminal $H_2{}^{16}O$ ligand at the metal in site 1. See Fig. S12 for spectra from DFT, Fig. S11 for underlying model structures, and Materials and Methods for computational procedures.

amplitudes, for example of the O_2/D_2O or $O_2/H_2{}^{18}O$ Fe/Fe and Mn/Fe samples and the OD/D_2O or $OH/H_2{}^{18}O$ labeled [FeFe] and [MnFe] cofactors, matched very well (i.e. within about ± 10%) (Fig. 8) so that quantitative comparison was feasible.

3.5. Assignment of cofactor isotope labeling patterns

Quantitative comparison was based on calculation of the root-mean-square deviation (rmsd) between the experimental and computational NRVS difference signals for all possible combinations of isotopic R2lox preparations and calculated cofactor labeling patterns. The matrices that resulted from inclusion of the QM/MM, (scaled) DFT, or mean computational data as well as of the [FeFe] or [MnFe] cofactor species in the calculations revealed essentially similar rmsd patterns with minima (smallest deviations between experimental and computational data) at similar positions (Fig. S16). This finding indicated that similar isotopic patterns were realized in the [FeFe] and [MnFe] cofactors in the R2lox protein. Therefore, mean rmsd values were calculated by averaging of the experimental data for the Fe/Fe and Mn/Fe preparations as well as of the computational data for the [FeFe] and [MnFe] cofactors, which facilitated assignment of the isotopic patterns in R2lox (Table 2, Fig. S17).

The rmsd was minimal for comparing the experimental values of the O_2/D_2O-labeled protein preparations to the calculated values of the OD/D_2O-labeled cofactors. This finding indicated that the protons both at the terminal water and the bridging hydroxide (μOH^-) were exchanged by deuterons upon protein solvation in heavy water. Small rmsd values for comparing the experimental values of the O_2/D_2O-labeled protein samples to some calculated $D/^{18}O$ double-labeled cofactor species are coincidental because there was no ^{18}O in these protein preparations. In particular, this holds for comparison with the $^{18}OH/H_2{}^{18}O$ cofactor species. The rmsd for comparison to the double-labeled species $^{18}OD/D_2{}^{18}O$ was larger, as expected due to the relatively large joint contributions to the NRVS difference amplitudes of ^{18}O in the hydroxo and water ligands. Comparison to the D-labeled species with ^{18}O either in the bridging hydroxo or terminal water ligand yielded comparably small rmsd values because for ^{18}O in $OD/D_2{}^{18}O$ or $^{18}OD/D_2O$, the labeled ligand contributes only relatively small NRVS difference amplitudes. In any event, the latter apparently good correlations are coincidental (no matter whether the rmsd is small), because there is no ^{18}O in the O_2/D_2O protein samples.

A unique rmsd minimum was observed when comparing the $O_2/H_2{}^{18}O$ protein data to the calculated $OH/H_2{}^{18}O$ cofactor data whereas much higher rmsd values resulted from comparison to the calculated $^{18}O_2/H_2O$ or $^{18}O_2/H_2{}^{18}O$ cofactor data (Table 2, Fig. S17). This result showed that the terminal water bound at iron in site 1 of the cofactor was exchanged with a $H_2{}^{18}O$ molecule from bulk water after formation of the Fe/Mn(III)Fe(III) cofactor by O_2 reduction, whereas the μOH^- mostly did not exchange with the solvent. Minimal rmsd values were found for comparison of the $^{18}O_2/H_2O$ proteins to the calculated OD/D_2O, $OD/D_2{}^{18}O$, and $^{18}OH/H_2O$ cofactors. The former two species were ruled out because there was no deuterium in these preparations. In these cases, relatively small rmsd values are obtained because the deuterium labeling adds only small NRVS difference amplitudes and the

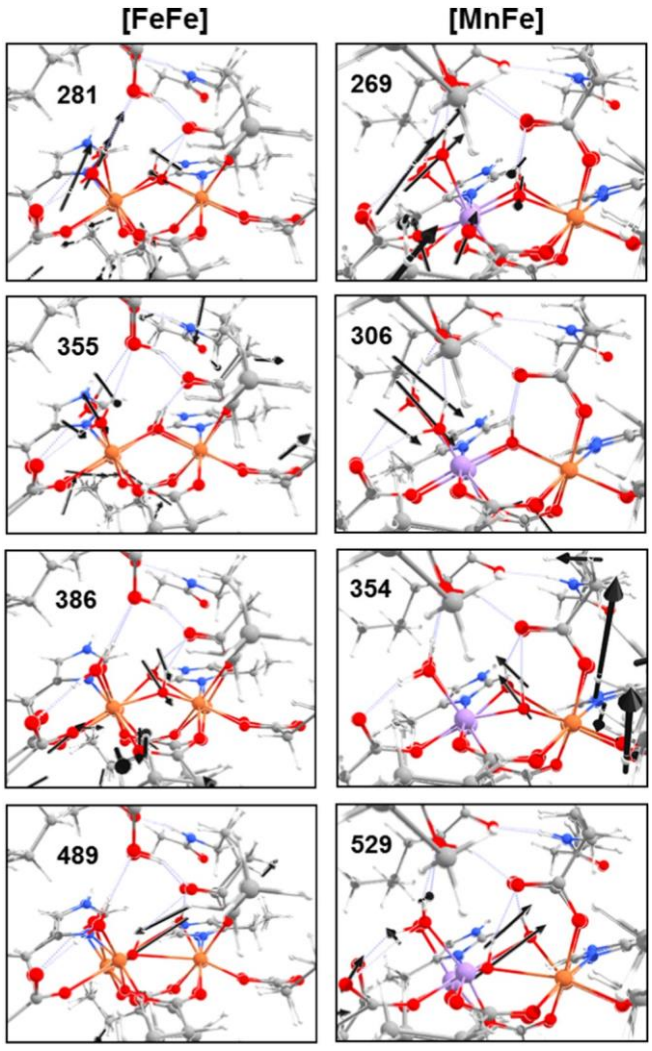

Fig. 7. Vibrational modes of [FeFe] and [MnFe] cofactors. Amplitudes and directions of atomic motions (arrows, not drawn to scale) in normal modes from QM/MM with prominent contributions from the μOH⁻ and H_2O ligands at the (unlabeled) [FeFe] (left) or [MnFe] (right) cofactors at given approximate frequencies (in cm^{-1}) are indicated; each panel shows an overlay of the two structures at the maximal deflection points of the O-atom vibrations of the two ligands. Color code: violet, Mn; orange, Fe; red, O; blue, N, grey, C; white, H.

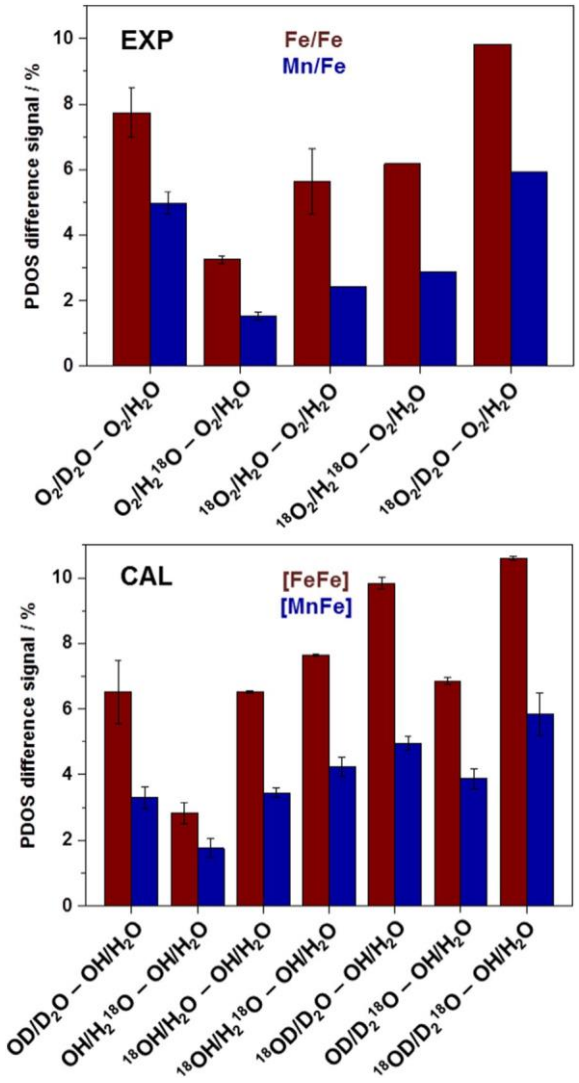

Fig. 8. Experimental and computational NRVS difference signals. Top: experimental NRVS (PDOS) difference signals for Fe/Fe and Mn/Fe R2lox (mean values over data from spectra in Figs. 4 and S8 where applicable, error bars show full signal ranges). Experimental difference signals were scaled to compensate for non-quantitative D_2O or $H_2{}^{18}O$ contents in the protein samples (see text); unscaled signals are shown in Fig. S14. Bottom: calculated NRVS (PDOS) difference signals for [FeFe] or [MnFe] cofactors in model structures with indicated isotopic labeling patterns. Signals represent mean values over QM/MM and scaled (x0.7) DFT data, error bars show full signal ranges; see Fig. S15 for individual (unscaled) data sets.

^{18}O labeling of the bridging hydroxide presumably was non-quantitative (see below). Comparison to the calculated $OH/H_2{}^{18}O$ and $^{18}OH/H_2{}^{18}O$ cofactors yielded larger rmsd values. These findings indicated that upon formation of the Fe/Mn(III)Fe(III) cofactor, one oxygen atom from (i.e., isotopically labeled) O_2 was incorporated in the μOH⁻. Because of its exchangeability as shown with $H_2{}^{18}O$, ^{18}O-labeling of the terminal water after $^{18}O_2$ reduction in unlabeled water was not expected and barely observed. For the $^{18}O_2/H_2{}^{18}O$ preparations, an overall similar distribution of rmsd minima as for the $^{18}O_2/H_2O$ preparations for comparison to the calculated ^{18}O-labeled cofactor species was observed, but the rmsd for the calculated $^{18}OH/H_2{}^{18}O$ cofactor species was significantly smaller for the $^{18}O_2/H_2{}^{18}O$ preparations (Table 2, Fig. S17). Accordingly, in the $^{18}O_2/H_2{}^{18}O$ protein samples both the terminal water and the μOH⁻ were ^{18}O-labeled. This observation strengthens our assignment that the terminal water exchanges with the bulk and one oxygen atom from O_2 is present in the hydroxide. The $^{18}O_2/D_2O$ protein preparations showed clear rmsd minima for comparison to the calculated $^{18}OD/D_2O$ and $^{18}OD/D_2{}^{18}O$ cofactor species. Because of its exchangeability (see above), persistent ^{18}O-labeling of the terminal water was not expected in heavy water, so that this result further corroborated inclusion of an oxygen atom from O_2 only in the hydroxide.

4. Discussion

The ligand-binding oxidase R2lox was employed to study reductive oxygen activation at [FeFe] and [MnFe] cofactors using nuclear resonance scattering. Aerobic in-vitro assembly facilitates high-yield incorporation of $^{57}Fe(III)^{57}Fe(III)$ or $Mn(III)^{57}Fe(III)$ cofactors in the protein, as revealed by TXRF and NFS in agreement with our earlier results [41,43,44,47,84]. Crystal structures have suggested that the trivalent metal sites are stabilized due to previous formation of a tyrosine-valine cross-link close to the cofactors [43–45]. These properties render R2lox a well-suited model system to evaluate the combination of X-ray vibrational spectroscopy (NRVS) and quantum chemical computations (QM/MM) as a tool for assigning the O_2 cleavage products at the

Table 2
Assignment of isotopic labeling patterns at the R2lox cofactors.[a]

Calculated PDOS difference signal	Experimental PDOS difference signal				
	O_2/D_2O – O_2/H_2O	$O_2/H_2{}^{18}O$ – O_2/H_2O	$^{18}O_2/H_2O$ – O_2/H_2O	$^{18}O_2/H_2{}^{18}O$ – O_2/H_2O	$^{18}O_2/D_2O$ – O_2/H_2O
	rmsd [%]				
OD/D_2O – OH/H_2O	1.5	2.5	0.7	0.2	3.2
$OH/H_2{}^{18}O$ – OH/H_2O	4.1	0.1	1.9	2.4	5.8
$^{18}OH/H_2O$ – OH/H_2O	1.4	2.6	0.8	0.3	3.1
$^{18}OH/H_2{}^{18}O$ – OH/H_2O	0.5	3.5	1.8	1.3	2.2
$^{18}OD/D_2O$ – OH/H_2O	1.0	5.0	3.2	2.7	0.7
$OD/D_2{}^{18}O$ – OH/H_2O	1.0	3.0	1.2	0.7	2.7
$^{18}OD/D_2{}^{18}O$ – OH/H_2O	1.8	5.8	4.1	3.5	0.1

[a] rmsd values (Eq. (4)) were calculated using data in Fig. 8 for all possible combinations of experimental and computational NRVS difference signals for the isotope-exchanged R2lox preparations (mean values over Fe/Fe and Mn/Fe species) and model structures (mean values over [FeFe] and [MnFe] cofactors and QM/MM and DFT data are shown, Fig. S17 shows a graphical data representation; for individual rmsd values for QM/MM and DFT data as well as for [FeFe] and [MnFe] cofactors see Fig. S16). rmsd minima correspond to apparent best agreement of experimental and computational data, white cells denote cofactor labeling-pattern assignments (dark-gray cells mark coincidental, i.e., excluded correlations; light-grey cells mark sub-optimal correlations; see text).

dimetal sites in isotope-labeled protein.

The NRVS spectra for Fe/Fe or Mn/Fe reconstituted R2lox with varying isotopic compositions showed intricate vibrational band patterns in a wide frequency range ($\lesssim$550 cm^{-1}), which are different for [FeFe] and [MnFe] cofactors [47], as well as relatively small band shifts (mostly $\lesssim$5 cm^{-1}) in the entire spectral range due to isotope exchange. The NRVS spectra include all vibrational modes with contributions from the ^{57}Fe nuclei, due to the lack of respective selection rule limitations, rendering them considerably more complex than, for example, Raman spectra of related dimetal systems [36,85–90]. In fact, the critical modes of, e.g., iron-oxygen interactions are not identified with distinct normal modes in the NRVS spectra, but these vibrations are mixed into a relatively large number of normal modes of the Fe/Fe and Fe/Mn cores. These properties preclude a direct ("fingerprinting") assignment of NRVS bands to specific vibrational modes of the metal ligands and of frequency shifts to isotope exchange patterns. Therefore, calculation of NRVS spectra is required for normal mode and isotope labeling assignment, which in turn mandates a reliable method for quantitative comparison of experimental and computational NRVS features. Here, we developed an approach based on quantification of NRVS difference spectra for correlation of vibrational band shifts. Good reproducibility of the expected NRVS difference signal ratios for a reference system, decent agreement of experimental and calculated signal amplitudes, as well as observation of similar signal patterns for Fe/Fe and Mn/Fe R2lox indicated that the method allows consistent analysis of NRVS data with reasonable sensitivity even for differing noise contributions and small frequency shifts.

Rigorous correlation of the experimental and computational NRVS signals has provided an unambiguous assignment of isotope exchange positions at the [FeFe] and [MnFe] cofactors in R2lox. We find that in the Mn/Fe(III)Fe(III) cofactors, the protons of the metal-bridging hydroxide (μOH^-) and of the terminal water (H_2O) ligand at the metal in site 1 exchange with the bulk solvent, which confirms the earlier determined protonation state of both ligands [42,47]. The H_2O ligand readily exchanges with the solvent. After exposure of R2lox containing divalent Mn/Fe ions to $^{18}O_2$, ^{18}O was found to be incorporated only in the μOH^- bridge. Accordingly, only one ^{18}O atom (μOH^-) from O_2 cleavage is detectable in the Mn/Fe(III)Fe(III) cofactors and from NRVS, there is no evidence for the fate of the second ^{18}O atom. In the R2lox crystal structures, mostly similar positions of water molecules at distances ≥7 Å to both metal sites were found for anaerobic Mn/Fe(II) and aerobic Mn/Fe(III) proteins [40,41,43–45,91], meaning that the additional O_2-derived water species can also not be localized in the structures of the oxidized proteins.

Earlier EPR experiments on R2lox, which did not address the location of the oxygen atoms from O_2, have shown incorporation of ^{17}O in the water ligand and (in part) in the bridging hydroxide in the Mn(III)Fe(III) cofactor formed in the presence of $^{16}O_2$ after buffer exchange to $H_2{}^{17}O$ [48]. The generally slightly smaller experimental NRVS difference signals for the $^{18}O_2/H_2O$ and $^{18}O_2/H_2{}^{18}O$ R2lox preparations in comparison to the calculated signals for the $^{18}OH/H_2O$ and $^{18}OH/H_2{}^{18}O$ cofactors may suggest that the μOH^- shows limited (~15%) exchange with bulk water within the duration of the buffer exchange also in the present experiments. Diminished exchange of the μOH^- with the solvent in the NRVS vs. EPR data likely is due mainly to a ~10-fold higher protein concentration in the buffer exchange procedure of the NRVS samples. In addition, the intrinsically small differences in the experimental NRVS data may result in a somewhat diminished sensitivity to the μOH^- exchange compared to EPR. These findings suggest that the H_2O ligand is replaced much faster (minutes) than the duration of the buffer exchange, whereas the decreased μOH^- replacement for an increased protein concentration at similar buffer exchange durations indicates much slower (hours) replacement of the μOH^- ligand.

Starting from R2lox with two divalent metal ions, exposure to O_2 and four-electron chemistry has been proposed to result in a transient μ-peroxo Mn/Fe(III)Fe(III) intermediate, followed by a Mn/Fe(IV)Fe(IV) state with two metal-bridging oxides at the cofactor [43,46], i.e., a "diamond core" configuration [30] (Fig. 9). Such species were inferred from spectroscopic data on similar enzymes and direct structural information for R2lox is not available. Similar diferric μ-peroxo as well as

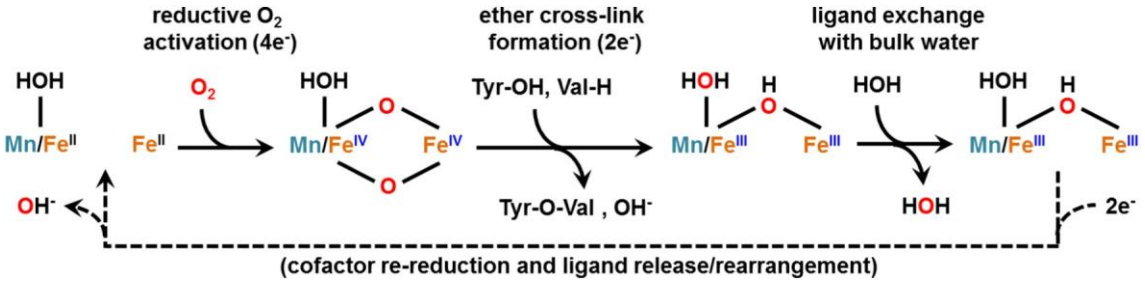

Fig. 9. Reductive O_2 activation at the R2lox cofactors. Four-electron reduction of O_2 is proposed to result in a Mn/Fe(IV)Fe(IV) diamond-core structure and two water species, followed by two-electron chemistry resulting in a tyrosine-valine ether cross-link and in the Mn/Fe(III)Fe(III) cofactors [41,43]. Exchange of the terminal water at Mn/Fe(III) in site 1 leads to the release of one water species to the bulk solvent, whereas the other O-atom from O_2 resides in the bridging hydroxide. The second water species from O_2 (μOH^-) would be released to the bulk mainly upon re-reduction of the cofactor to putatively initiate catalytic substrate reactions. Additional terminal and bridging (amino acid) ligands (see Fig. 1) are omitted for clarity.

diamond-core species, often based on Raman spectroscopy in isotope-exchange studies or crystallographic data, were proposed to occur during O_2 reduction at the diiron cofactors, e.g., in ferritin, soluble methane monooxygenase, R2 subunits of ribonucleotide reductases, chloramphenicol oxygenase, and stearoyl-ACP desaturase (see ref. [30] and refs. therein). In the latter enzymes, the high valent states are employed to oxidize external substrates or neighboring amino acids to yield reactive radical species. In R2lox, however, the putative Mn/Fe (IV)Fe(IV) species likely generates the Tyr-Val cross-link thereby leaving the stable Mn/Fe(III)Fe(III) cofactor (Fig. 9). This reaction was assigned to an activation process, but a suitable substrate for testing the enzyme activity is still missing. Such a substrate may bind at a similar metal-bridging position as the fatty acid that co-purifies with the R2lox protein [41,43]. The presence of only one bridging oxide in the Mn/Fe (III)Fe(III) cofactor implies that the second oxygen atom resulting from O_2 reduction leaves as water during cross-link formation. It is reasonable to assume that the μOH^- becomes protonated upon metal reduction so that it can replace the terminal water at the metal in site 1. One water molecule from O_2 reduction thereby is released directly into the solvent, whereas the other water (μOH^-) is mainly released after co- factor re-reduction (Fig. 9). The conditions for effective re-reduction that primes the enzyme for its actual catalytic reactions yet remain tobe elucidated. In summary, we show that site-selective and isotope-sensitive ^{57}Fe nuclear resonance X-ray scattering in combination with quantum chemistry facilitates assignment of structures due to reductive O_2 ac- tivation at a biological dimetal cofactor. Oxygen activation is a key topic in biology and chemistry, with many of the diverse reaction types involving iron centers (see ref. [92] for recent reviews). At present, however, the X-ray technique is available only at a handful of syn- chrotron sources. Inauguration of further experimental facilities may lead to a more central role of NRVS in the characterization of oxygen activation catalysts in the future.

Abbreviations

DFT density functional theory
R2lox R2-like ligand-binding oxidase from *Geobacillus kaustophilus*
NFS nuclear forward (X-ray) scattering
NRVS nuclear resonance vibrational (X-ray) spectroscopy
PDOS partial vibrational density of states
QM/MM quantum mechanics/molecular mechanics
TXRF total reflection X-ray

References

[1] D. Lundin, A.M. Poole, B.M. Sjoberg, M. Högbom, Use of structural phylogenetic networks for classification of the ferritin-like superfamily, J. Biol. Chem. 287 (2012)20565–20575.

[2] A. Yevenes, The ferritin superfamily, Subcell. Biochem. 83 (2017) 75–102.

[3] S.C. Andrews, The ferritin-like superfamily: evolution of the biological iron storeman from a rubrerythrin-like ancestor, Biochim. Biophys. Acta 1800 (2010)691–705.

[4] P. Nordlund, H. Eklund, Di-iron-carboxylate proteins, Curr. Opin. Struct. Biol. 5 (1995) 758–766.

[5] C.R. Bertozzi, C.J. Chang, B.G. Davis, M. Olvera de la Cruz, D.A. Tirrell, D. Zhao, Grand challenges in chemistry for 2016 and beyond, ACS Central Science 2 (2016) 1–3.

[6] J.A. Cotruvo Jr., J. Stubbe, Class I ribonucleotide reductases: metallocofactor assembly and repair in vitro and in vivo, Annu. Rev. Biochem. 80 (2011)19.11–19.35.

[7] A. Gräslund, M. Sahlin, Electron paramagnetic resonance and nuclear magnetic resonance studies of class I ribonucleotide reductase, Annu. Rev. Biophys. Biomol. Struct. 25 (1996) 259–286.

[8] D. Lundin, G. Berggren, D.T. Logan, B.M. Sjöberg, The origin and evolution of ribonucleotide reduction, Life 5 (2015) 604–636.

[9] M. Kolberg, K.R. Strand, P. Graff, K.K. Andersson, Structure, function, and mechanism of ribonucleotide reductases, Biochim. Biophys. Acta 1699 (2004) 1–34.

[10] C.E. Tinberg, S.J. Lippard, Dioxygen activation in soluble methane monooxygenase, Acc. Chem. Res. 44 (2011) 280–288.

[11] R. Banerjee, J.C. Jones, J.D. Lipscomb, Soluble methane monooxygenase, Annu. Rev. Biochem. (2019), https://doi.org/10.1146/annurev-biochem-013118-111529.

[12] M.O. Ross, A.C. Rosenzweig, A tale of two methane monooxygenases, J. Biol. Inorg. Chem. 22 (2017) 307–319.

[13] J.J. Griese, V. Srinivas, M. Hogbom, Assembly of nonheme Mn/Fe active sites in heterodinuclear metalloproteins, J. Biol. Inorg. Chem. 19 (2014) 759–774.

[14] S.J. Lange, L. Que Jr., Oxygen activating nonheme iron enzymes, Curr. Opin. Chem. Biol. 2 (1998) 159–172.

[15] A.J. Jasniewski, L. Que Jr., Dioxygen activation by nonheme diiron enzymes: di- verse dioxygen adducts, high-valent intermediates, and related model complexes, Chem. Rev. 118 (2018) 2554–2592.

[16] A.J. Komor, A.J. Jasniewski, L. Que, J.D. Lipscomb, Diiron monooxygenases in natural product biosynthesis, Natur. Prod. Rep. 35 (2018) 646–659.

[17] M. Högbom, Metal use in ribonucleotide reductase R2, di-iron, di-manganese and heterodinuclear–an intricate bioinorganic workaround to use different metals for the same reaction, Metallomics 3 (2011) 110–120.

[18] N. Voevodskaya, F. Lendzian, A. Ehrenberg, A. Graslund, High catalytic activity achieved with a mixed manganese-iron site in protein R2 of chlamydia ribonucleotide reductase, FEBS Lett. 581 (2007) 3351–3355.

[19] W. Jiang, D. Yun, L. Saleh, E.W. Barr, G. Xing, L.M. Hoffart, M.A. Maslak, C. Krebs, J.M. Bollinger Jr., A manganese(IV)/iron(III) cofactor in *Chlamydia trachomatis* ribonucleotide reductase, Science 316 (2007) 1188–1191.

[20] J.A. Cotruvo Jr., J. Stubbe, Metallation and mismetallation of iron and manganese proteins in vitro and in vivo: the class I ribonucleotide reductases as a case study, Metallomics 4 (2012) 1020–1036.

[21] M. Crona, E. Torrents, A.K. Rohr, A. Hofer, E. Furrer, A.B. Tomter, K.K. Andersson, M. Sahlin, B.M. Sjoberg, NrdH-redoxin protein mediates high enzyme activity in

manganese-reconstituted ribonucleotide reductase from Bacillus anthracis, J. Biol. Chem. 286 (2011) 33053–33060.

[22] A.K. Boal, J.A. Cotruvo Jr., J. Stubbe, A.C. Rosenzweig, The dimanganese(II) site of Bacillus subtilis class Ib ribonucleotide reductase, Biochemistry 51 (2012) 3861–3871.

[23] M.X. Huang, M.J. Parker, J. Stubbe, Choosing the right metal: case studies of class I ribonucleotide reductases, J. Biol. Chem. 289 (2014) 28104–28111.

[24] J.M. Bollinger Jr., W. Jiang, M.T. Green, C. Krebs, The manganese(IV)/iron(III) cofactor of *Chlamydia trachomatis* ribonucleotide reductase: structure, assembly, radical initiation, and evolution, Curr. Opin. Struct. Biol. 18 (2008) 650–657.

H.R. Rose, M.K. Ghosh, A.O. Maggiolo, C.J. Pollock, E.J. Blaesi, V. Hajj, Y.F. Wei,L.J. Rajakovich, W.C. Chang, Y.L. Han, M. Hajj, C. Krebs, A. Silakov, M.E. Pandelia,
J.M. Bollinger, A.K. Boal, Structural basis for superoxide activation of *Flavobacterium johnsoniae* class I ribonucleotide reductase and for radical initiation by its dimanganese cofactor, Biochemistry 57 (2018) 2679–2693.

[25] K. Roos, P.E. Siegbahn, Oxygen cleavage with manganese and iron in ribonucleotide reductase from *Chlamydia trachomatis*, J. Biol. Inorg. Chem. 16 (2011) 553–565.

[26] W. Zhu, B.M. Tackett, J.G. Chen, F. Jiao, Bimetallic electrocatalysts for CO2 reduction, Top. Curr. Chem. 376 (2018) 41.

[27] Z. Bian, S. Das, M.H. Wai, P. Hongmanorom, S. Kawi, A review on bimetallic nickel-based catalysts for CO2 reforming of methane, Chemphyschem 18 (2017) 3117–3134.

[28] D.R. Pye, N.P. Mankad, Bimetallic catalysis for C-C and C-X coupling reactions, Chem. Sci. 8 (2017) 1705–1718.

[29] L. Que, W.B. Tolman, Bis(mu-oxo)dimetal "diamond" cores in copper and iron complexes relevant to biocatalysis, Angew. Chem. Int. Ed. 41 (2002) 1114–1137.

[30] W. Nam, Dioxygen activation by metalloenzymes and models, Acc. Chem. Res. 40 (2007) 465.

[31] M. Bennati, F. Lendzian, M. Schmittel, H. Zipse, Spectroscopic and theoretical approaches for studying radical reactions in class I ribonucleotide reductase, Biol. Chem. 386 (2005) 1007–1022.

[32] C.J. Chang, M.C.Y. Chang, N.H. Damrauer, D.G. Nocera, Proton-coupled electron transfer: a unifying mechanism for biological charge transport, amino acid radical initiation and propagation, and bond making/breaking reactions of water and oxygen, Biochim. Biophys. Acata 1655 (2004) 13–28.

[33] J.T. Groves, High-valent iron in chemical and biological oxidations, J. Inorg. Biochem. 100 (2006) 434–447.

[34] B.J. Brazeau, J.D. Lipscomb, Electron transfer and radical forming reactions of methane monooxygenase, Subcell. Biochem. 35 (2000) 233–277.

[35] R. Banerjee, A.J. Komor, J.D. Lipscomb, Use of isotopes and isotope effects for investigations of diiron oxygenase mechanisms, measurement and analysis of kinetic isotope effects, Meth. Enzymol. 596 (2017) 239–290.

[36] P. Nordlund, A. Aberg, U. Uhlin, H. Eklund, Crystallographic investigations of ribonucleotide reductase, Biochem. Soc. Trans. 21 (Pt 3) (1993) 735–738.

[37] R.R. Crichton, J.P. Declercq, X-ray structures of ferritins and related proteins, Biochim. Biophys. Acta 1800 (2010) 706–718.

[38] E.G. Kovaleva, M.B. Neibergall, S. Chakrabarty, J.D. Lipscomb, Finding intermediates in the O2 activation pathways of non-heme iron oxygenases, Acc. Chem. Res. 40 (2007) 475–483.

[39] Y. Kutin, V. Srinivas, M. Fritz, R. Kositzki, H.S. Shafaat, J. Birrell, E. Bill, M. Haumann, W. Lubitz, M. Hogbom, J.J. Griese, N. Cox, Divergent assembly mechanisms of the manganese/iron cofactors in R2lox and R2c proteins, J. Inorg. Biochem. 162 (2016) 164–177.

[40] J. Griese, R. Kositzki, P. Schrapers, R. Branca, A. Nordström, J. Lehtiö, M. Haumann, M. Högbom, Structural basis for oxygen activation at a heterodinuclear Mn/Fe cofactor, J. Biol. Chem. 290 (2015) 25254–25272.

[41] H.S. Shafaat, J.J. Griese, D.A. Pantazis, K. Roos, C.S. Andersson, A. Popovic-Bijelic, A. Graslund, P.E. Siegbahn, F. Neese, W. Lubitz, M. Hogbom, N. Cox, Electronic structural flexibility of heterobimetallic Mn/Fe cofactors: R2lox and R2c proteins, J.Am. Chem. Soc. 136 (2014) 13399–13409.

[42] J.J. Griese, K. Roos, N. Cox, H.S. Shafaat, R.M. Branca, J. Lehtio, A. Graslund, W. Lubitz, P.E. Siegbahn, M. Hogbom, Direct observation of structurally encoded metal discrimination and ether bond formation in a heterodinuclear metalloprotein, Proc. Natl. Acad. Sci. U. S. A. 110 (2013) 17189–17194.

[43] J.J. Griese, R. Kositzki, M. Haumann, M. Högbom, Assembly of a heterodinuclear Mn/Fe cofactor is coupled to tyrosine-valine ether cross-link formation in the R2-like ligand-binding oxidase, J. Biol. Inorg. Chem. (2019), https://doi.org/10.1007/s00775-019-01639-4.

[44] J.J. Griese, R.M.M. Branca, V. Srinivas, M. Hogbom, Ether cross-link formation in the R2-like ligand-binding oxidase, J. Biol. Inorg. Chem. 23 (2018) 879–886.

[45] E.K. Miller, N.E. Trivelas, P.T. Maugeri, E.J. Blaesi, H.S. Shafaat, Time-resolved investigations of heterobimetallic cofactor assembly in R2lox reveal distinct Mn/Fe intermediates, Biochemistry 56 (2017) 3369–3379.

[46] R. Kositzki, S. Mebs, J. Marx, J.J. Griese, N. Schuth, M. Högbom, V. Schünemann, M. Haumann, Protonation state of MnFe and FeFe cofactors in a ligand binding oxidase revealed by X ray absorption, emission, and vibrational spectroscopy and QM/MM calculations, Inorg. Chem. 19 (2016) 9869–9885.

[47] L. Rapatskiy, W.M. Ames, M. Perez-Navarro, A. Savitsky, J.J. Griese, T. Weyhermuller, H.S. Shafaat, M. Hogbom, F. Neese, D.A. Pantazis, N. Cox, Characterization of oxygen bridged manganese model complexes using multi-frequency O-17-hyperfine EPR spectroscopies and density functional theory, J. Phys. Chem. B 119 (2015) 13904–13921.

[48] F. Siebert, P. Hildebrandt, Vibrational Spectroscopy in Life Science, Wiley-VCH, Berlin, 2008.

[49] R. Rüffer, Nuclear resonance scattering, in: H. Saleem (Ed.), Reference Module in Materials Science and Materials Engineering, Elsevier, Amsterdam, 2016, pp. 1–13.

[50] W.R. Scheidt, S.M. Durbin, J.T. Sage, Nuclear resonance vibrational spectroscopy -NRVS, J. Inorg. Biochem. 99 (2005) 60–71.

[51] W. Sturhahn, Nuclear resonant spectroscopy, J. Phys. Condens. Matt. 16 (2004) S497–S530.

[52] H. Wang, E.E. Alp, Y. Yoda, S.P. Cramer, A practical guide for nuclear resonance vibrational spectroscopy (NRVS) of biochemical samples and model compounds, Meth. Mol. Biol. 1122 (2014) 125–137.

[53] L.B. Gee, H.X. Wang, S.P. Cramer, NRVS for Fe in biology: experiment and basic interpretation, Fe-S cluster enzymes, Meth. Enzymol. 599 (2018) 409–425.

[54] J. Marx, V. Srinivas, I. Faus, H. Auerbach, L. Scherthan, K. Jenni, A.I. Chumakov, R. Rüffer, M. Högbom, M. Haumann, V. Schünemann, Nuclear inelastic scattering at the diiron center of ribonucleotide reductase from *Escherichia coli*, Hyperfine Interact. 238 (82) (2017) 1–10.

[55] K. Park, E.I. Solomon, Modeling nuclear resonance vibrational spectroscopic data of binuclear non-heme iron enzymes using density functional theory, Canad. J. Chem. 92 (2014) 975–978.

[56] Y. Kwak, W. Jiang, L.M.K. Dassama, K. Park, C.B. Bell, L.V. Liu, S.D. Wong, M. Saito, Y. Kobayashi, S. Kitao, M. Seto, Y. Yoda, E.E. Alp, J.Y. Zhao, J.M. Bollinger, C. Krebs, E.I. Solomon, Geometric and electronic structure of the Mn(IV)Fe(III) cofactor in class Ic ribonucleotide reductase: correlation to the class Ia binuclear non-heme iron enzyme, J. Am. Chem. Soc. 135 (2013) 17573–17584.

[57] U. Vanburck, D.P. Siddons, J.B. Hastings, U. Bergmann, R. Hollatz, Nuclear forward scattering of synchrotron radiation, Phys. Rev. B 46 (1992) 6207–6211.

[58] F. Paulat, T.C. Berto, S. DeBeer George, L. Goodrich, V.K. Praneeth, C.D. Sulok, N. Lehnert, Vibrational assignments of six-coordinate ferrous heme nitrosyls: new insight from nuclear resonance vibrational spectroscopy, Inorg. Chem. 47 (2008) 11449–11451.

[59] N. Lehnert, J.T. Sage, N. Silvernail, W.R. Scheidt, E.E. Alp, W. Sturhahn, J. Zhao, Oriented single-crystal nuclear resonance vibrational spectroscopy of [Fe(TPP)(MI)(NO)]: quantitative assessment of the trans effect of NO, Inorg. Chem. 49 (2010) 7197–7215.

[60] G. Winter, Iron(II) halides, in: A. Wold, J.K. Ruff (Eds.), Inorganic Syntheses, Willey, New York, 1973, pp. 101–104.

[61] R. Klockenkämper, Total Reflection X-Ray Fluorescence Analysis, Wiley-VCH, London, UK, 1996.

[62] R. Rüffer, A.I. Chumakov, Nuclear resonance beamline at ESRF, Hyperfine Interact. 97-8 (1996) 589–604.

[63] S. Mebs, R. Kositzki, J. Duan, L. Kertess, M. Senger, F. Wittkamp, U.P. Apfel,

T. Happe, S.T. Stripp, M. Winkler, M. Haumann, Hydrogen and oxygen trapping at the H-cluster of [FeFe]-hydrogenase revealed by site-selective spectroscopy and QM/MM calculations, Biochim. Biophys. Acta 1859 (2018) 28–41.

[64] S. Mebs, J. Duan, F. Wittkamp, S.T. Stripp, T. Happe, U.-P. Apfel, M. Winkler, M. Haumann, Differential protonation at the catalytic six-iron cofactor of [FeFe]-hydrogenases revealed by ^{57}Fe nuclear resonance scattering and QM/MM analysis, Inorg. Chem. 58 (2019) 4000–4013.

[65] A. Chumakov, R. Rüffer, Nuclear inelastic scattering, Hyperfine Interact 113 (1998) 59–79.

[66] A.I. Chumakov, A.Q.R. Baron, R. Ruffer, H. Grunsteudel, H.F. Grunsteudel, A. Meyer, Nuclear resonance energy analysis of inelastic x-ray scattering, Phys. Rev.Lett. 76 (1996) 4258–4261.

[67] H. Paulsen, V. Schunernann, A.X. Trautwein, H. Winkler, Mössbauer studies ofcoordination compounds using synchrotron radiation, Coord. Chem.Rev. 249 (2005) 255–272.

[68] G.V. Smirnov, General properties of nuclear resonant scattering, Hyperfine Interact. 123 (1999) 31–77.

[69] M. Miglierini, M. Pavlovic, V. Prochazka, T. Hatala, G. Schumacher, R. Rüffer, Evolution of structure and local magnetic fields during crystallization of HITPERM glassy alloys studied by in situ diffraction and nuclear forward scattering of synchrotron radiation, Phys. Chem. Chem. Phys. 17 (2015) 28239–28249.

[70] A.X. Trautwein, H. Winkler, S. Schwendy, H. Grunsteudel, W. Meyer-Klaucke, O. Leupold, H.D. Ruter, E. Gerdau, M. Haas, E. Realo, D. Mandon, R. Weiss, Iron porphyrins reinvestigated by a new method: Mössbauer spectroscopy using synchrotron radiation, Pure Appl. Chem. 70 (1998) 917–924.

[71] B. Sepiol, A. Meyer, G. Vogl, R. Ruffer, A.I. Chumakov, A.Q.R. Baron, Time domain study of Fe-57 diffusion using nuclear forward scattering of synchrotron radiation, Phys. Rev. Lett. 76 (1996) 3220–3223.

[72] T. Vreven, K. Morokuma, O. Farkas, H.B. Schlegel, M.J. Frisch, Geometry optimization with QM/MM, ONIOM, and other combined methods. I. Microiterations and constraints, J. Comput. Chem. 24 (2003) 760–769.

[73] S. Dapprich, I. Komaromi, K.S. Byun, K. Morokuma, M.J. Frisch, A new ONIOM implementation in Gaussian98. Part I. The calculation of energies, gradients, vibrational frequencies and electric field derivatives, J. Mol. Struc. Theo. Chem. 461 (1999) 1–21.

[74] M.J.T. Frisch, G. W.; Schlegel, H. B.; Scuseria, G. E.; Robb, M. A.; Cheeseman, J. R.; Scalmani, G.; Barone, V.; Mennucci, B.; Petersson, G. A.; Nakatsuji, H.; Caricato, M.; Li, X.; Hratchian, H. P.; Izmaylov, A. F.; Bloino, J.; Zheng, G.; Sonnenberg, J. L.; Hada, M.; Ehara, M.; Toyota, K.; Fukuda, R.; Hasegawa, J.; Ishida, M.; Nakajima, T.; Honda, Y.; Kitao, O.; Nakai, H.; Vreven, T.; Montgomery, J. A., Jr.; Peralta, J. E.; Ogliaro, F.; Bearpark, M.; Heyd, J. J.; Brothers, E.; Kudin, K. N.; Staroverov, V. N.; Kobayashi, R.; Normand, J.; Raghavachari, K.; Rendell, A.; Burant, J. C.; Iyengar, S. S.; Tomasi, J.; Cossi, M.; Rega, N.; Millam, J. M.; Klene, M.; Knox, J. E.; Cross, J. B.; Bakken, V.; Adamo, C.; Jaramillo, J.; Gomperts, R.; Stratmann, R. E.; Yazyev, O.; Austin, A. J.; Cammi, R.; Pomelli, C.; Ochterski, J. W.; Martin, R. L.; Morokuma, K.; Zakrzewski, V. G.; Voth, G. A.; Salvador, P.; Dannenberg, J. J.; Dapprich, S.; Daniels, A. D.; Farkas, Ö.; Foresman, J. B.; Ortiz, J. V.; Cioslowski, J.; Fox, D. J., Gaussian 09, Revision D.01., Gaussian, Inc., Wallingford CT., (2009).

[75] C. Lee, W. Yang, R.G. Parr, Development of the Colle-Salvetti correlation-energy formula into a functional of the electron density, Phys. Rev. B 37 (1988) 785–789.

[76] A.D. Becke, A new mixing of Hartree-Fock and local density-functional theories, J. Chem. Phys. 98 (1993) 1372–1377.

[77] F. Weigend, R. Ahlrichs, Balanced basis sets of split valence, triple zeta valence and quadruple zeta valence quality for H to Rn: design and assessment of accuracy, Phys. Chem. Chem. Phys. 7 (2005) 3297–3305.

[78] M. Senger, S. Mebs, J. Duan, O. Shulenina, K. Laun, L. Kertess, F. Wittkamp, U.-P. Apfel, T. Happe, M. Winkler, M. Haumann, S.T. Stripp, Protonation and reduction dynamics at the hydrogen-forming cofactor of [FeFe]-hydrogenases, Phys. Chem. Chem. Phys. 20 (2017) 3128–3140.